Simulation of the polar cap potential during periods with northward interplanetary magnetic field

S. K. Bhattarai,[1] R. E. Lopez,[1] R. Bruntz,[1] J. G. Lyon,[2] and M. Wiltberger[3]

Received 8 September 2011; revised 28 February 2012; accepted 1 March 2012; published 21 April 2012.

[1] In this paper we examine the response of the ionospheric cross-polar cap potential to steady, purely northward interplanetary magnetic field (IMF) using the Lyon-Fedder-Mobarry global magnetohydrodynamic simulation of the Earth's magnetosphere. The simulation produces the typical, high-latitude "reversed cell" convection that is associated with northward IMF, along with a two cell convection pattern at lower latitude that we interpret as being driven by the viscous interaction. The behavior of the potential can be divided into two basic regions: the viscous dominated region and the reconnection dominated region. The viscous dominated region is characterized by decreasing viscous potential with increasing northward IMF. The reconnection dominated region may be further subdivided into a linear region, where reconnection potential increases with increasing magnitude of northward IMF, and the saturation region, where the value of the reconnection potential is relatively insensitive to the magnitude of the northward IMF. The saturation of the cross-polar cap potential for northward IMF has recently been documented using observations and is here established as a feature of a global MHD simulation as well. The region at which the response of the potential transitions from the linear region to the saturation region is also the region in parameter space at which the magnetosheath transitions from being dominated by the plasma pressure to being dominated by the magnetic energy density. This result is supportive of the recent magnetosheath force balance model for the modulation of the reconnection potential. Within that framework, and including our current understanding of the viscous potential, we present a conceptual model for understanding the full variation of the polar cap potential for northward IMF, including the simulated dependencies of the potential on solar wind speed and ionospheric conductivity.

Citation: Bhattarai, S. K., R. E. Lopez, R. Bruntz, J. G. Lyon, and M. Wiltberger (2012), Simulation of the polar cap potential during periods with northward interplanetary magnetic field, *J. Geophys. Res.*, *117*, A04219, doi:10.1029/2011JA017143.

1. Introduction

[2] The circulation of plasma and magnetic field lines within the magnetosphere due to the influence of electromagnetic and/or mechanical force is called plasma convection. Plasma convection in the magnetosphere is mainly due to magnetic merging [*Dungey*, 1961] and viscous interaction [*Axford and Hines*, 1961]. Merging is generally considered to be the dominant mechanism for producing the circulation of magnetospheric plasma driven by solar wind stress, thus transferring energy and momentum from the solar wind into the geospace system.

[3] The viscous interaction is due to the velocity shear that exists between the magnetosheath and magnetospheric plasma lying inside the magnetopause. This velocity shear drives Kelvin-Helmholtz waves [e.g., *Otto and Fairfield*, 2000; *Claudepierre et al.*, 2008] that cause plasma at the vicinity of magnetopause to move antisunward, which is in turn balanced by a return flow occurring closer to Earth, forming a convection cell pattern. This viscous cell maps down to the ionosphere producing antisunward flow at high latitude and a return sunward flow at lower latitudes. This flow means that there must be a self-consistent electric field in the frame of reference fixed to the (nonrotating) Earth, and an associated electric potential across the ionosphere [e.g., *Vasyliūnas*, 2001], which we refer to as the viscous potential (VP). The orientation of convection cells produced due to viscous interaction is independent of interplanetary magnetic field (IMF) orientation.

[4] Magnetic merging between the geomagnetic field and the IMF also produces convection cells called the reconnection convection cells but the orientation of the reconnection cell varies with the orientation of the IMF. When the IMF is purely southward, the magnetic reconnection occurs along the dayside equatorial region, which is followed by the draping of reconnected field lines to the nightside because of

[1]Department of Physics, University of Texas at Arlington, Arlington, Texas, USA.
[2]Department of Physics and Astronomy, Dartmouth College, Hanover, New Hampshire, USA.
[3]High Altitude Observatory, National Center for Atmospheric Research, Boulder, Colorado, USA.

0148-0227/12/2011JA017143

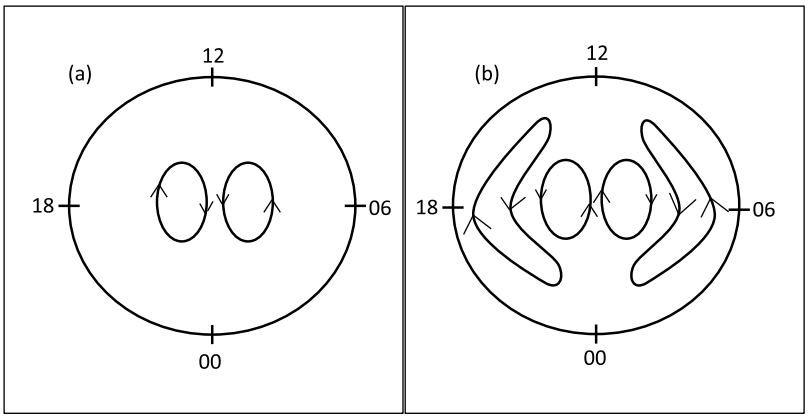

Figure 1. A schematic of the two cell and four cell convection patterns for (a) southward and (b) northward interplanetary magnetic field (IMF), respectively.

magnetosheath flow. These draped field lines reach the tail lobes where merging of the north and south magnetic tail lobe occur along the nightside equatorial region [*Dungey*, 1961]. The magnetic flux stored in the tail because of the nightside reconnection for southward IMF is typically released in the form of a substorm [e.g., *Baker et al.*, 1996]. The phenomenology of substorms has been extensively examined using both observations [e.g., *Baker et al.*, 1993; *Lopez et al.*, 1994] and simulations [e.g., *Lyon et al.*, 1998]. Substorms are reasonably well understood on the global scale, though there are many details about substorm initiation and evolution that are still controversial [*Angelopoulos et al.*, 2008, 2009; *Lui*, 2009]. If the IMF remains strongly southward for extended periods of time magnetic storms occur [e.g., *Gonzalez et al.*, 1994] and the continuous Dungey cycle of flux circulation leads to the intensification of the ring current [e.g., *Lopez et al.*, 2009], while weaker steady driving may produce a steady magnetospheric convection event [e.g., *DeJong et al.*, 2007].

[5] For purely southward IMF, the dynamos creating the viscous and reconnection cells are oriented in the same direction, producing a two cell convection pattern [*Hill*, 1994] as illustrated in Figure 1, with the viscous component of the convection cells located entirely on closed field lines. The two cell convection pattern for southward IMF has been illustrated by *Ruohoniemi and Greenwald* [1996] using HF radar observations. This two cell convection pattern is associated with the large-scale Region 1 Birkeland current system that is directed into the ionosphere on the dawn side and out of the ionosphere on the dusk side [e.g., *Iijima and Potemra*, 1976]. The magnetic shear comprising the Region 1 Birkeland current system represents the transmission of the solar wind stresses into the ionosphere via the merging and viscous interaction mechanisms. The lower-latitude Region 2 current is driven by the pressure gradients in the inner magnetosphere [e.g., *Wolf*, 1995].

[6] In the case when IMF is northward, magnetic reconnection occurs poleward of the cusp region, as illustrated in Figure 2. *Hill* [1994] reviewed different theoretical models of polar cap convection for the case of northward IMF. *Watanabe and Sofko* [2009] proposed that the basic magnetic flux circulation cycle for the northward IMF with finite B_y consists of IMF-lobe reconnection in one hemisphere and a lobe-closed field line reconnection in the other. However, for the northward IMF, the stress that is delivered to the ionosphere is oppositely directed to that produced by the southward IMF. Thus magnetic reconnection for northward IMF produces reconnection cells with a sunward flow at higher latitude followed by an antisunward flow at lower latitude. These cells are called the reverse convection cells. *Sundberg et al.* [2009a] investigated the reconnection potential in reverse convection portion of the four cell convection patterns using DMSP observations, while the potential in the boundary layer (the viscous potential) in the lower-latitude cells for the northward IMF was examined by *Sundberg et al.* [2009b].

[7] The viscous and reverse convection cells together form a four cell convection pattern [e.g., *Burke et al.*, 1979; *Crooker*, 1992; *Cumnock et al.*, 1995] for the northward IMF (see Figure 1b). The existence of the four cell convection pattern for the northward IMF was also examined by *Huang et al.* [2000] using SuperDARN data. Along with Region 1 and Region 2 current systems, an additional current system called the NBZ current system appears in the geospace system for the northward IMF [*Iijima and Potemra*, 1976]. The NBZ current is located poleward of the Region 1 current, occurs on open field lines, and has a Region 2 polarity [*Iijima and Shibaji*, 1987]. Although we have a rough sketch of different current systems and the convection cells created when the IMF is northward, the dynamics of the convection pattern in the case of northward IMF is still less understood compared to southward IMF [*Watanabe and Sofko*, 2009].

[8] The interaction between the IMF and geomagnetic field causes mass, momentum and energy to be transferred from the solar wind to the Earth's magnetosphere-ionosphere system. A key measure of the coupling is the measurement of the magnitude of cross-polar cap potential (CPCP). The CPCP is a measure of the difference between the highest and lowest value of potential in the polar cap region. When the IMF is purely southward, analysis of the simulation results show that the CPCP is the sum of viscous potential and reconnection potential [*Lopez et al.*, 2010, 2012; *Bruntz et al.*, 2012]. Hence measuring the CPCP is a method of

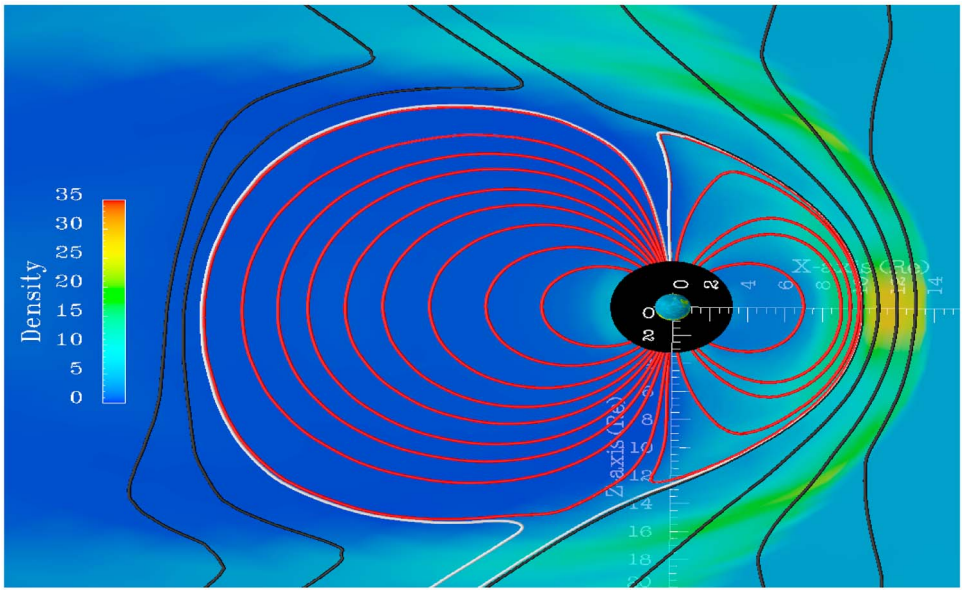

Figure 2. Visualization of the Lyon-Fedder-Mobarry (LFM) simulation results in the *X-Z* plane showing the high-latitude reconnection topology during purely northward IMF (10 nT). The Sun is on the right side of the picture. Solar wind field lines, reconnected field lines, and closed field lines are drawn in black, white, and red color, respectively, and the plasma density is color coded.

measuring the total amount of coupling between the solar wind and the magnetosphere when the IMF is southward.

[9] In the case of northward IMF, the plasma convection patterns in the viscous and reconnection cells are oppositely oriented. Hence, the measurement of the CPCP (the maximum potential minus the minimum potential) is not a measure of the total magnetosphere-ionosphere coupling and it is not just the sum of the viscous and merging potentials. Instead it is a generally a measure of either the viscous potential or the reconnection potential, as illustrated in Figure 3. When the viscous potential is larger, the CPCP will be a measure of viscous interaction, but when the merging potential is larger, the CPCP will be a measure of merging interaction. And in some cases, if there is a significant asymmetry between the dawn and dusk values of the potential (due, for example, to an east-west component

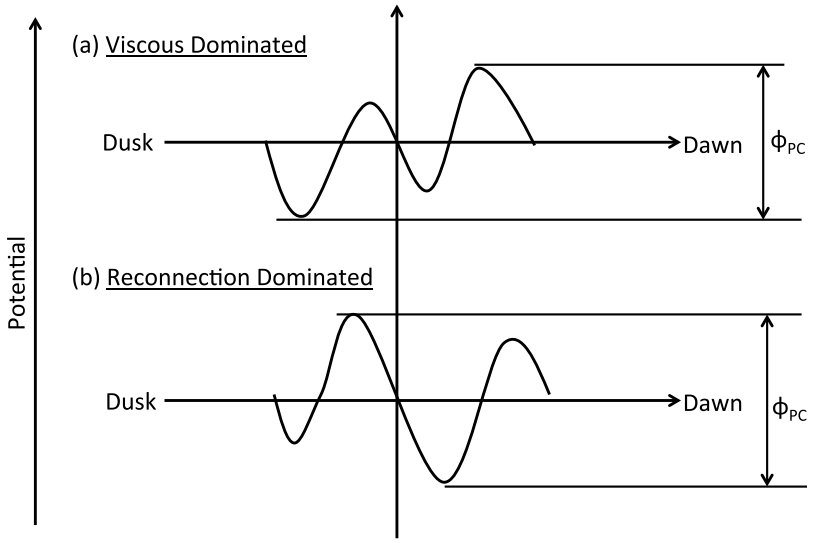

Figure 3. A schematic of the variation of the potential across the ionosphere from dawn to dusk during northward IMF. Since the cross-polar cap potential (CPCP) is defined as the maximum potential minus the minimum potential, this value can correspond either to the viscous potential (at the low-latitude edge of the potential pattern) or the merging potential (at the high-latitude center of the potential pattern), depending on which one is greater.

of the IMF), the CPCP could in fact represent the difference between the max (or min) of the viscous potential and the min (or max) of the merging potential. Hence it would not be a good measure of magnetospheric convection or any other particular process that produces convection. However, in the simulation results presented below we use purely northward IMF with steady solar wind to drive the simulation, thus avoiding this issue.

[10] Since typically reconnection is the dominant solar wind–magnetosphere coupling processes, the CPCP generally responds to the IMF magnitude and orientation, as well as to ionospheric conductivity. In particular, for southward IMF, the CPCP increases with increasing magnitude of B_z. However, this increase does not continue for large IMF magnitudes; at some point the CPCP become insensitive to further increase in the IMF magnitude. The CPCP is saturated when it stops responding to an increasing magnitude of southward B_z. The saturation of the CPCP has been reported by many different authors for strongly southward IMF using different approaches, for example, assimilated mapping of ionospheric electrodynamics (AMIE) reconstructions of ionospheric potentials [*Russell et al.*, 2001; *Liemohn et al.*, 2002], high-latitude radar observations of ionospheric flows [*Shepherd et al.*, 2002] and DMSP drift meter measurements [*Hairston et al.*, 2003; *Ober et al.*, 2003]. Moreover, ionospheric potential saturation for southward IMF has also been identified in various global MHD models [e.g., *Raeder et al.*, 2001] including the Lyon-Fedder-Mobarry (LFM) simulation code [*Merkine et al.*, 2003; *Lopez et al.*, 2009, 2010]. The saturation of the CPCP for large northward IMF has also been reported by *Wilder et al.* [2008, 2009, 2010], using ground-based radar observations, and by *Sundberg et al.* [2009a], using DMSP satellite data. In particular, *Sundberg et al.* [2009a] reported a saturation value of the reconnection potential of about 60 kV, and that the saturation effect becomes apparent when the IMF B_z is between 10 and 15 nT. The saturation of the CPCP for large east-west oriented IMF has also been shown by *Mitchell et al.* [2010].

[11] In this paper we examine the response of the CPCP for northward IMF in the Lyon-Fedder-Mobarry global MHD simulation. We will explore how the simulated CPCP depends on the solar wind and ionospheric conditions across the entire range of IMF magnitudes (northward), from 0 nT up to large values and will present a consistent and coherent explanation for the overall behavior of the CPCP throughout the IMF range. In particular, we will demonstrate that simulation exhibits saturation of the CPCP for large values of the IMF, where "large" means that the magnetosheath becomes magnetically dominated. This is consistent with the magnetosheath force balance model proposed by *Lopez et al.* [2010]. Other features of the behavior of the CPCP will be shown to be consistent with the force balance model as well, both for saturation and for periods when there is no saturation.

2. The Lyon-Fedder-Mobarry Simulation

[12] We use the Lyon-Fedder-Mobarry (LFM) global MHD simulation model [*Lyon et al.*, 2004] with a grid size of $50 \times 24 \times 32$. The LFM code solves the time-dependent 3-D single fluid MHD equations in a distorted spherical grid. The LFM grid extends from +25 R_E to -300 R_E along the X direction and +100 to -100 R_E along Y and Z directions, with the origin of the coordinate system located at the center of the Earth. All the results obtained in this paper from LFM simulation correspond to purely northward IMF ($B_x = B_y = 0$) with zero dipole tilt and a solar wind density of 5 cm^{-3}. All LFM runs were initialized with -5 nT B_z for 2 hours, followed by +5 nT B_z for six more hours. Then the desired value of northward IMF was introduced for 16 more hours, for a total of 24 hours. Runs were performed for constant ionospheric Pedersen conductivities of 5, 10, and 20 mhos, with zero Hall conductivity. Runs were also performed using the LFM empirical ionosphere initialized with a F10.7 flux of 100 (see *Fedder et al.* [1995] for details on the conductivity model), which leads to nonuniform conductivities around 3–5 mhos.

[13] The ionospheric potential in LFM grid is obtained by solving the current continuity equation,

$$\nabla \cdot (\Sigma \cdot \nabla \phi) = j_{\parallel} \sin \delta, \tag{1}$$

where Σ is the conductivity tensor δ is the dip angle, $j_{\parallel}$ is the field aligned current per unit area and ϕ is the ionospheric electrostatic potential to be solved. In the case of constant, uniform conductance, equation (1) reduces to a simple Poisson equation for the potential. The conductivity tensor for the LFM simulation with constant ionospheric conductivity as shown in equation (1) is a uniform height-integrated conductance, whereas in the case of conductance model with solar extreme ultraviolet (EUV) irradiance and auroral precipitation input, the total conductance is taken as the square root of the sum of the squares of the conductivities due to electron precipitation and EUV flux during the simulation period. [*Fedder et al.*, 1995; *Lyon et al.*, 2004]. For our LFM runs, the inner boundary of the MHD domain was set at 3 R_E. The inner boundary is the location where the ionosphere gets coupled with the magnetosphere. Below 3 R_E, the Birkeland current is mapped directly to ionosphere, where equation (1) is solved to calculate the electric field. This field is mapped back to the inner boundary to calculate boundary conditions for plasma flow in the MHD domain. All CPCP steady state values calculated here have been averaged from 14:00 to 16:00 simulation time. Results obtained from the LFM simulation were analyzed using CISM-DX [*Wiltberger et al.*, 2005]. The LFM code has been successfully used to model a wide range of magnetospheric phenomena, including real events [e.g., *Lyon et al.*, 1998; *Lopez et al.*, 1999, 2007], so we have confidence that the global features of the potential described here correspond to the behavior of the real magnetosphere.

3. Four Cell Convection Pattern in the LFM Simulation

[14] Results obtained from the LFM global MHD simulation model demonstrate the existence of a symmetric four cell convection pattern, shown in Figure 4, which is what is expected for purely northward IMF. This result has been known for many years, along with the fact that the LFM produces the NBZ current system [e.g., *Fedder and Lyon*, 1995]. All images in Figure 4 are presented from a view looking down from above the northern polar region with the Sun at the bottom of the page. All of the cases correspond to

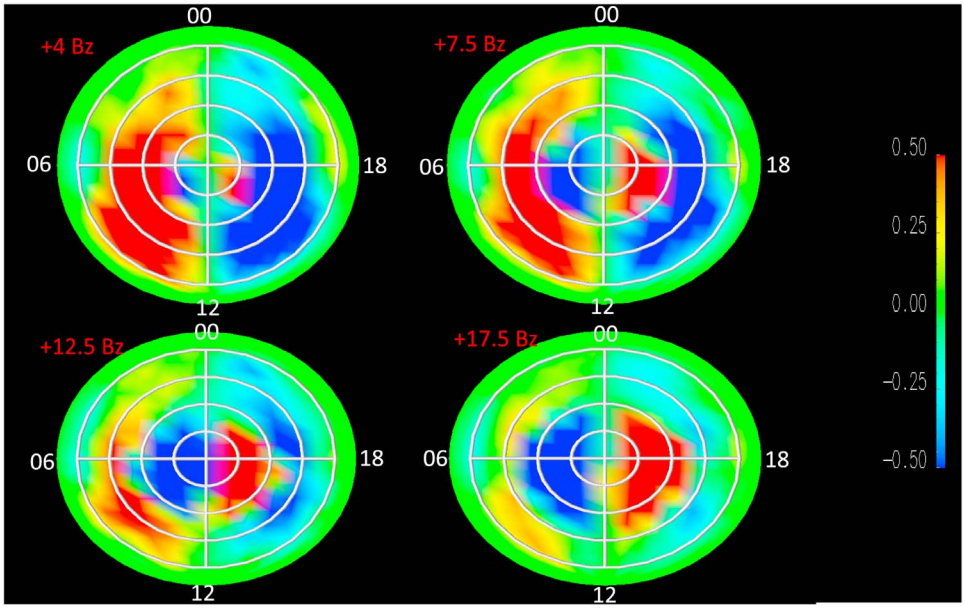

Figure 4. Four cell convection pattern seen in LFM simulation for purely northward IMF. The view is from above the North Pole with Sun at the bottom of the page. B_z is in units of nT. The value of the potential ranges from −0.5 to +0.5 kV in order to visualize the evolution of reconnection cell with increasing B_z. Each white circle is at an angle of 10° from the Pole.

the simulations with a solar wind velocity of 400 km/s, a density of 5 cm^{-3} and a constant ionospheric Pedersen conductivity of 10 mhos.

[15] The potential in these images have only been shown in range of −0.5 to +0.5 kV so that a larger size of the colored cell implies a greater extent of the convection cell, which in turn implies a stronger convection pattern. The blue and red colors represent negative and positive potential values, respectively. The image on top left corner is a result obtained for a solar wind magnetic field of +4 nT B_z showing the dominant viscous cells at lower latitudes with smaller reconnection cells (with reversed potential) at higher latitudes. As the magnitude of the northward IMF increases, the size and magnitude of the reconnection cells increases until the reconnection cells dominate over the viscous cells. For an IMF value of +17.5 nT B_z, we see that the reconnection cell is overwhelmingly dominant over the viscous cell. The increase in the size of reconnection cell with increasing northward B_z produces an equatorward shift in both the open-closed field line boundary and the location of viscous cell. This is consistent with the fact that viscous cells are generated in the closed field line region. Furthermore, we also found that the peaks of reconnection and viscous cells do not overlap for northward IMF suggesting that the decrease in viscous potential value is to a larger extent, independent of increase in reconnection potential. We will discuss in detail about the location of the maxima and minima of the convection cells and the dynamics involved for northward IMF in another issue.

4. Dependence of the Cross-Polar Cap Potential on Northward IMF

[16] Figure 3 shows a schematic of how the value of the CPCP (max minus min) reflects the actual convection pattern for two opposite cases: one where the viscous potential dominates and one where the merging potential dominates. This is important for understanding how the CPCP behaves as a function of B_z. Figure 5 shows the dependence of the CPCP on B_z for three solar wind velocities with three different (uniform, constant) ionospheric Pedersen conductances, plus a set of simulation with the empirical ionosphere module [*Lyon et al.*, 2004] initialized with a F10.7 value of 100 (all runs have the same solar wind density of 5 cm^{-3}). The LFM runs with $V_x = -400$ km/s includes IMF B_z values only up to 22.5 nT. The runs with B_z greater than 22.5 nT resulted in the bow shock forming beyond the edge of the LFM grid because of the very low Mach number and hence were not taken into consideration. The higher solar wind velocity runs include IMF B_z values as large as 40 nT (the higher solar wind velocity allows for larger magnetic fields since the only requirement is that the Mach number be such that the shock forms within the LFM simulation domain). While there are occasionally some odd variations in the potential as B_z increases, such as the anomalously high CPCP for the simulation with $V = 600$ km/s (Figure 5b) when the $B_z = 15$ nT (a result that we currently do not understand), the CPCP overall follows a generally consistent pattern of variation as a function of B_z for the range of velocities and ionospheric conductivities presented.

[17] Another interesting result we see in Figure 5 (and Figure 6) is that the total polar cap potential in the LFM simulation starts to decrease with increasing northward B_z, reaches a minimum value, and then starts to increase again. At lower values of B_z (i.e., $B_z < 4$ nT) the viscous potential is greater than the reconnection potential, but with increasing B_z, the CPCP (which is in fact measuring the viscous potential in that range of B_z) decreases, indicating an inverse relationship between the magnitude of the viscous potential and magnitude of northward B_z. This is quite different than

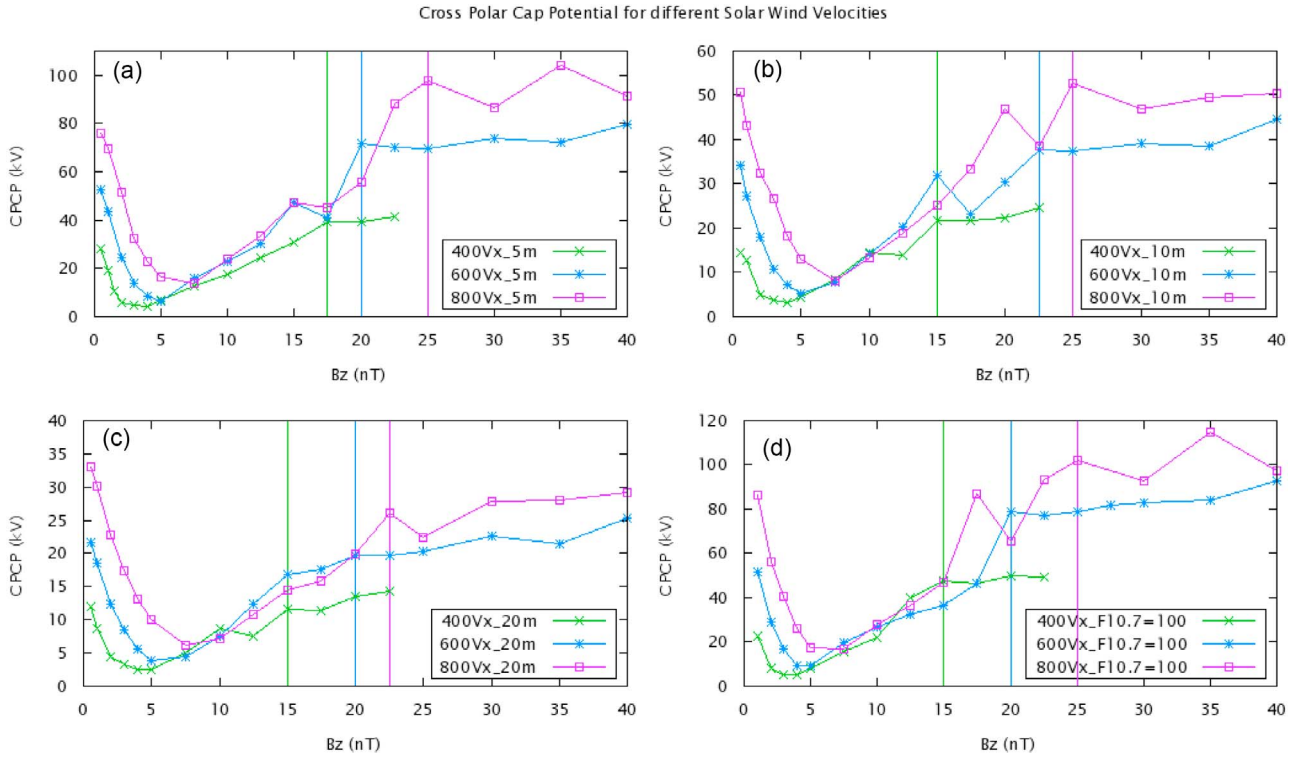

Figure 5. Results obtained from LFM simulation showing the variation of the CPCP as a function of IMF B_z for various solar wind velocities. (a–c) CPCP for uniform ionospheric conductivities of 5, 10, and 20 mhos. (d) Results using the LFM ionospheric conductivity module initialized with $F_{10.7} = 100$. The vertical lines separate the linear regime from the saturation regime, as discussed in the text.

the case for southward IMF where the magnitude of the viscous potential is independent of the magnitude of the (purely) southward IMF [*Lopez et al.*, 2010; *Bruntz et al.*, 2012]. Thus, as discussed by *Lopez et al.* [2012], the viscous potential apparently weakens with increasing northward IMF. Once the reconnection potential is greater than viscous potential, the CPCP (which then becomes a measure of the merging rate) starts to increase with increasing B_z and finally reaches saturation. Figures 5 and 6 also show that value of B_z where the magnitude of the reconnection potential exceeds that of the viscous potential increases with increasing solar wind velocity. This is understandable since the viscous potential increases with increasing solar wind velocity, as discussed by *Newell et al.* [2008] as well as *Bruntz et al.* [2012]. Thus for larger solar wind speeds, a larger merging potential produced by a larger northward IMF is required in order for the merging potential to exceed the magnitude of the viscous potential.

[18] When the merging potential is larger than the viscous potential Figure 5 shows that the CPCP grows with increasing IMF magnitude. However, after a certain value of B_z, the CPCP does not continue to respond much to increasing value of B_z, indicating saturation of the CPCP for northward IMF. We can clearly see that all those plots show saturation of the CPCP. Thus the MHD simulation is reproducing the behavior reported by *Wilder et al.* [2008, 2009] and by *Sundberg et al.* [2009a]. The region where the CPCP decreases for an increasing value of B_z will henceforth be called the viscous-dominated region, while the region where the potential starts to increase and finally becomes insensitive to increasing value of northward B_z will henceforth be called the reconnection-dominated region. The reconnection-dominated region has further been subdivided into the linear regime where the CPCP increases with increasing northward B_z, and the saturation regime where the CPCP is insensitive to increasing northward B_z. Vertical lines of respective colors have been drawn in all plots of Figure 5 to separate the linear regime from the saturation regime.

5. Saturation, the Geoeffective Length, and Magnetosheath Force Balance

[19] The solar wind flow carries a large amount of flux past the Earth, but obviously only a small fraction of the flux actually merges with the geomagnetic field. This fraction can be expressed as a length perpendicular to the solar wind flow and the IMF, denoting the amount of flux that actually crosses the merging line. This is the geoeffective length [*Burke and Maynard*, 1999; *Lopez et al.*, 2010], which is much smaller than the cross section of the magnetosphere, and even smaller for the northward IMF as compared to the southward IMF because of the relative inefficiency of merging for the northward IMF. The reconnection potential can be represented as $\Phi_r = V_x B_z L_G$, where L_G is the geoeffective length.

[20] Figure 6 shows the CPCP as a function of IMF magnitude with each plot representing one velocity and four ionospheric conductivities (all runs have the same density).

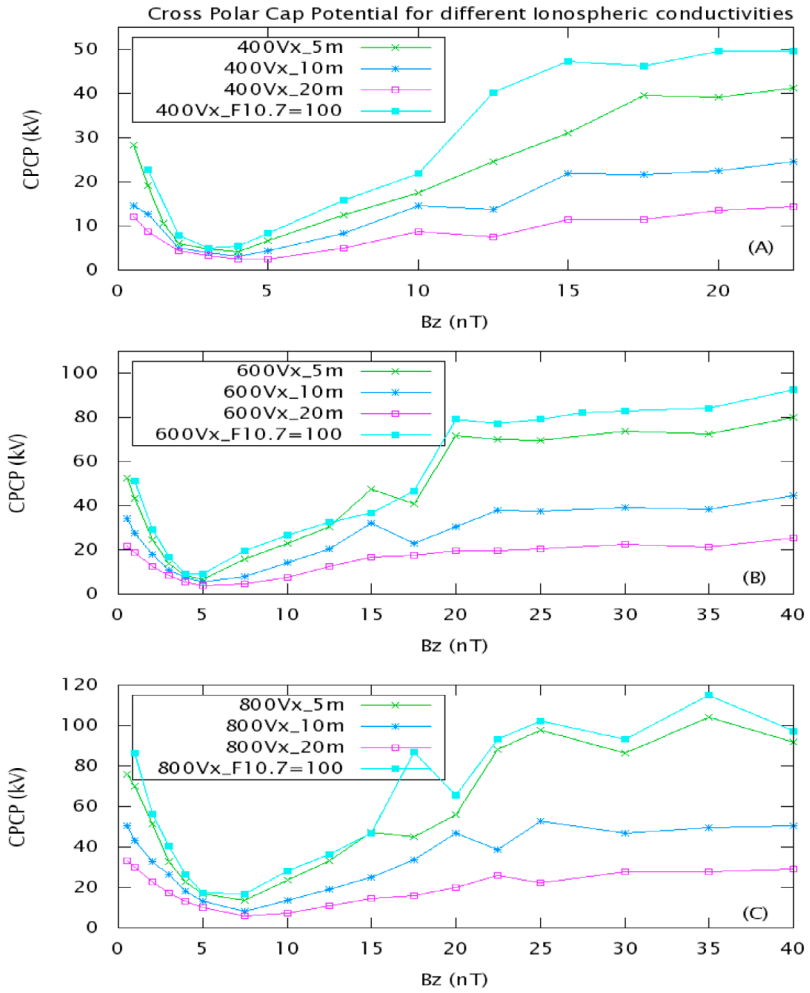

Figure 6. The variation of the CPCP versus B_z for three constant solar wind velocities but various conductivities. Figure 6 uses the same results as Figure 5, but they are organized differently.

Given that the solar wind velocity is constant for each set of simulations, the various slopes of the CPCP as a function of B_z in the linear reconnection-dominated regions of Figures 5 and 6 correspond to the geoeffective lengths for those solar wind plasma and ionospheric conductivity conditions, with a larger slope being a longer length. Inspecting Figure 5 we see that the slopes of the lines in the linear region do not appear to be linearly dependent on velocity for fixed density and ionospheric conductivity, which leads us to a seemingly odd conclusion. To get an actual length one must divide the slope (which is in units of kV/nT) by the solar wind speed. Thus for the slopes in Figure 5 to be less than linearly dependent (refer to Table 1) on solar wind speed means that the geoeffective length must be decreasing as the solar wind speed increases. *Lopez et al.* [2010], by examining the behavior of the CPCP for southward IMF, arrived at that same conclusion that the geoeffective length is smaller for larger solar wind speeds in the linear regime, and we will return to this issue later.

[21] A second thing that is evident from Figure 6 is that when the IMF becomes large enough, the CPCP stops responding very much to additional increase in the IMF. This phenomenon of saturation, documented in the observational literature as discussed above, means that when the IMF reaches some magnitude, the amount of solar wind flux that is merged per unit time must be limited. Thus when the CPCP saturates, the geoeffective length must begin to vary inversely proportional to the IMF so that the reconnection

Table 1. Variation of Geoeffective Length for Different Values of Solar Wind Velocities and Ionospheric Conductivities

	Slope of the Linear Regime (kV/nT)			Geoeffective Lengths (Re)		
Solar Wind Velocity (km/s)	5 mhos	10 mhos	20 mhos	5 mhos	10 mhos	20 mhos
400	2.44	2.04	0.8	0.96	0.80	0.31
600	3.19	2.45	1.18	0.83	0.64	0.3
800	3.91	2.54	1.28	0.77	0.50	0.25

potential is constant, for example, $\Phi_r = V_x B_z L_G \approx V_x B_z (L_s B_s / B_z)$, where L_s is the geoeffective length at the saturation value of the IMF, B_s . We note that for a typical solar wind velocity of 400 km/s, the IMF value at which the saturation occurred is the same value (10–15 nT) as determined by *Sundberg et al.* [2009a]. We also note that the saturation value of the CPCP (in this case identical to the reconnection potential as illustrated in Figure 3) is in the same neighborhood as the 60 kV reconnection saturation potential identified by *Sundberg et al.* [2009a]. Inspecting Figure 6, it can be seen that the saturation potential increases with increasing solar wind velocity. The saturation potential is also larger for smaller ionospheric conductivity. These are features of saturation for southward IMF as well [e.g., *Lopez et al.*, 2010, and references therein].

[22] A number of physical explanations have been proposed to account for the phenomenon of saturation of the CPCP for southward IMF. These include the weakening of the dayside field by the Region 1 currents [*Hill et al.*, 1976; *Siscoe et al.*, 2002a, 2002b], the development of Alfvén wings during low solar wind Alfvén Mach number flows [*Ridley*, 2007; *Kivelson and Ridley*, 2008], configuration changes on the dayside that could choke off merging [*Raeder et al.*, 2001], or changes in the magnetopause shape and magnetosheath thickness [*Merkine et al.*, 2003; *Merkin et al.*, 2007]. All of these models predict features like larger saturation potentials for larger solar wind velocities and lower ionospheric conductivity that are evident in the simulations presented here.

[23] More recently, *Lopez et al.* [2010] introduced the magnetosheath force balance model, aspects of which have a relationship to the some of the other proposed causes for saturation, especially the perspective of *Merkine et al.* [2003] and *Merkin et al.* [2007]. However, the Lopez model is the only one that treats the variation of the geoeffective length across the entire range of IMF magnitudes so that CPCP saturation is simply a consequence of the same physics that operates in the linear region. The Siscoe-Hill model is based on the idea that when the dayside field is significantly weakened by the Birkeland current, saturation will occur in order to limit the Birkeland current [*Siscoe et al.*, 2002a]. Another version of the model is that the Birkeland current (and the potential) is limited by the amount of Birkeland current needed to stand off the solar wind pressure through the $\boldsymbol{J}\times\boldsymbol{B}$ force [*Siscoe et al.*, 2002b]. Both versions require a critical Birkeland current value to produce saturation. Given the less efficient reconnection for the northward IMF, *Siscoe et al.* [2002a] predicted saturation at much higher value of the IMF for northward IMF, since the magnetosphere under the northward IMF is a less efficient generator and it would take a larger solar wind electric field to produce the critical amount of Birkeland current. However, we see that the value of the potential and the Birkeland current system during saturation of the northward IMF is smaller than that for the southward IMF both in simulations and in observations [e.g., *Wilder et al.*, 2010], thus the Siscoe-Hill argument as currently formulated cannot be correct. The Alfvén wing model does not suffer this limitation, but it only operates during very low Alfvén Mach number flows. Moreover, that model provides no insight into the behavior of the geoeffective length for values of IMF B_z less than needed for saturation in the regime where the full solar wind potential drop across the magnetosphere is no being applied, but the potential is linearly dependent on the solar wind electric field.

[24] On the other hand, unexpected results such a dependence of the geoeffective length on velocity for small IMF B_z is easily understood in the context of the Lopez force balance model. For typical IMF values (<6 nT), the solar wind has a large Mach number and the compression ratio across the bow shock does not depend strongly on upstream conditions, it is basically a factor of four [e.g., *Lopez et al.*, 2004]. So while the magnetosheath plasma density is independent of the solar wind velocity, the magnetosheath plasma pressure is not since most of the kinetic energy of the solar wind appears as thermal energy downstream of the shock. Thus as the solar wind velocity increases, the plasma pressure and the pressure gradient force on the magnetosheath flow increases while the inertia of the flow does not increase. This results in a greater divergence of the flow around the magnetospheric obstacle, which should produce a shorter geoeffective length for larger solar wind velocity in the nonsaturation regime where the potential is linearly dependent on the IMF.

[25] Table 1 shows the slope of the potential versus B_z and the corresponding geoeffective lengths obtained from the slopes in Figures 5 and 6 in the linear reconnection-dominated regime for different values of solar wind velocity and ionospheric conductivities. What can be seen is that the geoeffective length does decrease somewhat with increasing solar wind velocity for all ionospheric conductivities. For ionospheric conductivity of 5 and 20 mhos, the geoeffective length decreases by a factor of 1.25 as the solar wind velocity goes up by a factor of 2. For 10 mhos, the geoeffective length decreases by a factor of 1.6 for the same 400 km/s to 800 km/s increase in solar wind velocity. Thus there does seem to be a decrease in the geoeffective length as the solar wind velocity increases, though the trend is not linear. Hence the reconnection potential will still increase with increasing solar wind speed for a fixed northward IMF value. This is similar to the result found for purely southward IMF by *Lopez et al.* [2010], though the decrease in the geoeffective length as a function of velocity is less as compared to the southward IMF situation.

[26] According to the Lopez force balance model, the point at which saturation effects begin to be seen should be when the magnetic force begins to dominate over the pressure gradient force in the magnetosheath. Figure 7 presents a plot of β, the ratio of the plasma pressure to the magnetic pressure, in the magnetosheath for two different velocities at three values of the purely northward IMF (all runs have a uniform 10 mho conductance). For the simulations with a solar wind speed of 400 km/s we see that in the linear region (IMF B_z = 7.5 nT) β is greater than 1 throughout the magnetosheath, but in the saturation region (IMF B_z = 17.5 nT) it is clearly less than one. The transition region between the two behaviors (IMF B_z = 12.5 nT, as can be seen in Figures 5 and 6) is also the transition from as plasma-dominated magnetosheath to a magnetically dominated one. For solar wind velocity of 800 km/s, however, we see that plasma beta is still greater than one for B_z = 17.5 nT showing that the transition from the linear to saturation regime for higher velocity occurs at a higher value of solar wind B_z. Table 2

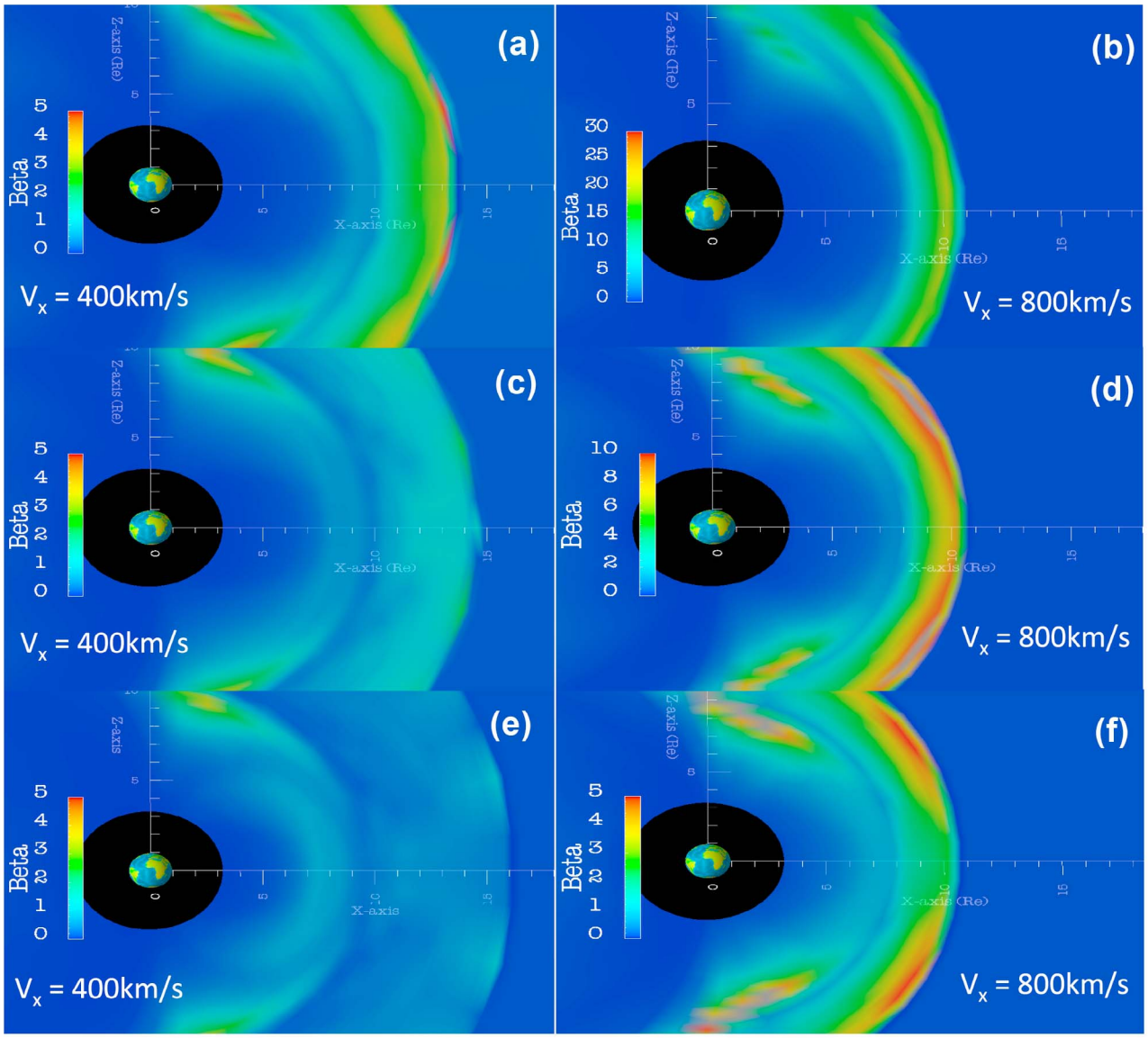

Figure 7. Visualization of the plasma beta in the *X-Z* plane for cases with purely northward IMF with magnitudes of (a, b) 7.5 nT, (c, d) 12.5 nT, and (e, f) 17.5 nT for two different solar wind velocities. Both runs have a solar wind density of 5 cm^{-3} and a uniform ionospheric conductance of 10 mhos.

shows range of solar wind B_z values between which the magnetosphere transitions from pressure dominated to magnetically dominated magnetosheath as determined from the simulation runs. The values obtained in Table 2 were obtained by looking at the *X-Z* cut plane image of the magnetosphere as in Figure 7 and is seen to be consistent with the values we would obtain from Figures 5 and 6.

[27] Above explanation holds true for other solar wind velocities as well. The point at which saturation effects are seen is marked by a transition from a magnetosheath where

Table 2. Range of Solar Wind B_z Values When the Magnetosheath Transitions From Pressure Dominated to Magnetically Dominated Regime for Different Values of Solar Wind Speed and Ionospheric Conductivities

	Values of B_z When the Magnetosheath Beta Transitions From Being Greater Than One to Less Than One During Different Ionospheric Conductivities			
Solar Wind Velocity (km/s)	5 mhos	10 mhos	20 mhos	F10.7 = 100
400	12.5–15	12.5–15	12.5–15	10–12.5
600	17.5–20	17.5–20	15–17.5	15–17.5
800	20–22.5	22.5–25	20–22.5	20–22.5

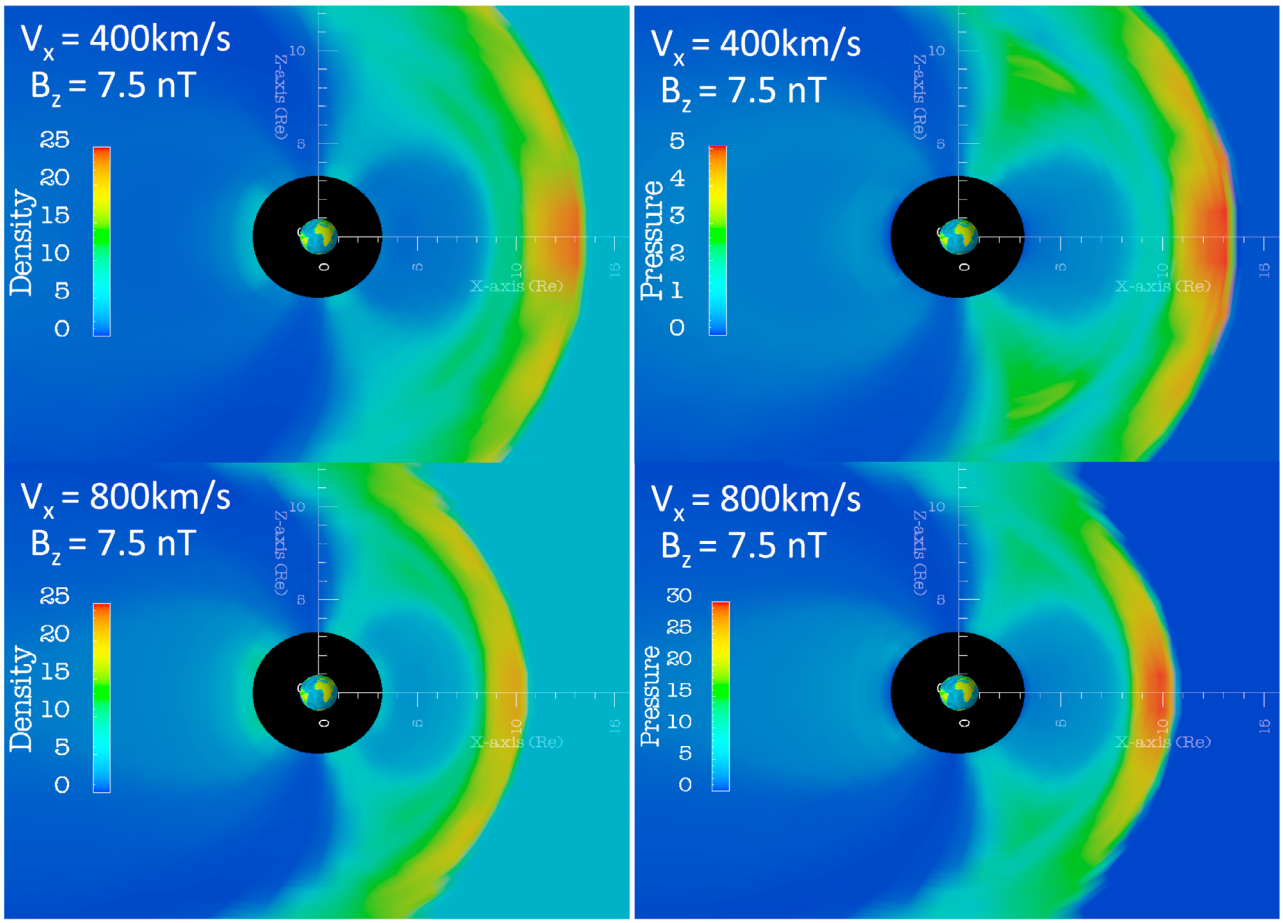

Figure 8. Visualization of the plasma density and pressure in the *X-Z* plane for cases with 7.5 nT purely northward IMF for two different solar wind velocities. Both runs have a solar wind density of 5 cm^{-3} and a uniform ionospheric conductance of 10 mhos.

the plasma pressure gradient is the largest force on the flow to a magnetosheath where the $\boldsymbol{J}\times\boldsymbol{B}$ force is the largest force on the flow. Inspecting Figure 7 for the results of simulations with high solar wind velocity (800 km/s), we see that the magnetosheath is dominated by plasma pressure when B_z = 12.5 nT, and Figure 6 shows that at that value of the IMF, the potential is in the linear region. When B_z = 17.5 nT, we see that the magnetosheath is beginning to approach β = 1 in some regions, just as the potential begins to approach the saturation region. We also see in Figure 6 that the value of B_z for which CPCP saturates increases with increasing velocity. The force balance argument is that as the solar wind velocity increases, so does the magnetosheath plasma pressure. Thus for higher solar wind velocities, a higher value of IMF B_z is required before the magnetosheath can become magnetically dominated, leading to a larger saturation potential. This can readily be seen in Figure 8, which contrasts a lower velocity simulation (400 km/s) with a higher velocity (800 km/s) simulation, with all other factors unchanged. Note that the color scales are different for the lower and upper panels comparing density and pressure in order to show the range in each case. The same effects occur at various values of ionospheric conductivity as well.

[28] Another feature of the force balance model is that it explains the shorter geoeffective length for larger ionospheric conductivity in the linear reconnection-dominated regime where the reconnection potential dominates. This occurs in the northward IMF simulations, as seen in Table 1. As in the case for southward IMF, a more conducting ionosphere leads to a greater change in the shape of the magnetosphere [e.g., *Merkine et al.*, 2003; *Lopez et al.*, 2010], which affects the flow. Figure 9 shows the effect when considering two runs with identical solar wind density, velocity and IMF. In these two cases the IMF B_z is set to 7.5 nT, well into the reconnection-dominated linear regime where the CPCP is a measure of the merging potential, but not affected by saturation. The flow that reaches the postcusp northward IMF merging line is at high Z values, but for that flow the magnetosheath plasma pressure, and hence the force on the flow diverting away from the merging region, is greater for the higher conductivity case. Thus the geoeffective length should be shorter and the merging potential should be smaller for the high conductivity case. This is the behavior supported by the simulation results in Table 1 over the range of solar wind velocities. Thus the force balance model [*Lopez et al.*, 2010] provides a coherent conceptual framework for explaining for

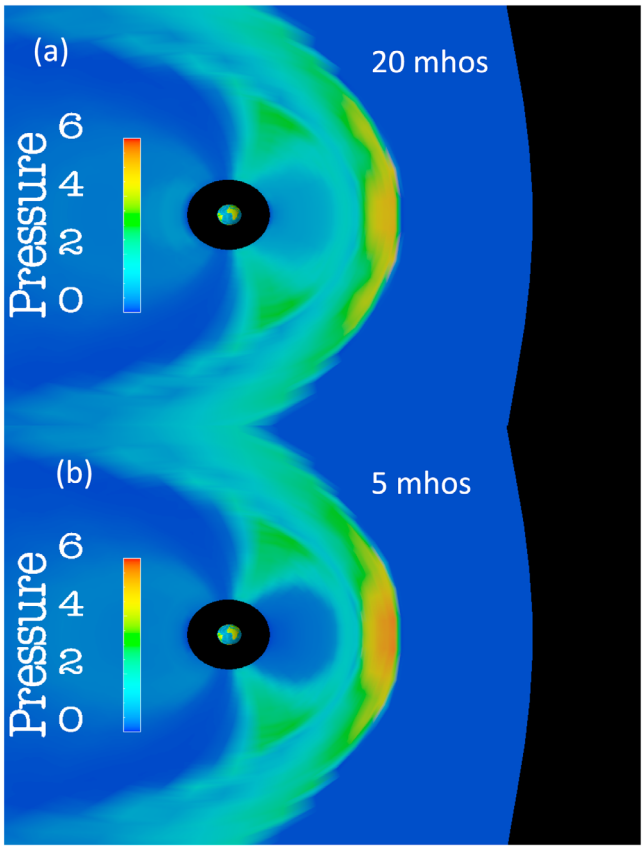

Figure 9. Visualization of the plasma pressure for cases with 7.5 nT purely northward IMF for uniform ionospheric conductances of (a) 20 mhos and (b) 5 mhos. Both runs have a solar wind density of 5 cm^{-3} and a solar wind velocity of 400 km/s.

the dependence of the reconnection potential at all values of northward IMF B_z (not just saturation values) for the range of velocities and ionospheric conductivities examined in this paper.

6. Conclusions

[29] We have examined the behavior of the polar cap potential in the Lyon-Fedder-Mobarry MHD simulation in response to various values of northward IMF for different values of ionospheric conductance and solar wind velocity. We find a consistent behavior of the CPCP as a function of the solar wind driver. There are two regions of response: the viscous dominated region where the viscous potential decreases linearly (for the most part) to increasing IMF magnitude, and a reconnection dominated region. The reconnection dominated region is in turn split into a region where the CPCP increases with increasing northward B_z and saturation region where the CPCP does not respond to increasing northward B_z. We find that the viscous potential decreases with increasing northward IMF and that the merging potential increases with increasing northward IMF, at least until saturation. Finally, the overall behavior of the reconnection potential as a function of IMF magnitude, solar wind velocity, and ionospheric conductivity can be understood over the entire IMF range in terms of the magnetosheath force balance model proposed by *Lopez et al.* [2010].

[30] **Acknowledgments.** This paper is based on work supported by CISM, which is funded by the STC Program of the National Science Foundation under agreement ATM-0120950, NASA grant NNX09AI63G, and NSF grant ATM-0900920. The National Center for Atmospheric Research is sponsored by the National Science Foundation. The authors acknowledge helpful conversations with E. Mitchell and R. Wilder.

[31] Masaki Fujimoto thanks the reviewers for their assistance in evaluating this paper.

References

Angelopoulos, V., et al. (2008), Tail reconnection triggering substorm onset, *Science*, *321*, 931–935, doi:10.1126/science.1160495.

Angelopoulos, V., et al. (2009), Response to comment on "Tail reconnection triggering substorm onset," *Science*, *324*, 1391, doi:10.1126/science.1168045.

Axford, W. I., and C. O. Hines (1961), A unifying theory of high-latitude geophysical phenomena and geomagnetic storms, *Can. J. Phys.*, *39*, 1433–1464, doi:10.1139/p61-172.

Baker, D. N., T. I. Pulkkinen, R. L. McPherron, J. D. Craven, L. A. Frank, R. D. Elphinstone, J. S. Murphree, J. F. Fennel, R. E. Lopez, and T. Nagai (1993), CDAW 9 analysis of magnetospheric events on May 3, 1986: Event C, *J. Geophys. Res.*, *98*(A3), 3815–3834, doi:10.1029/92JA02475.

Baker, D. N., T. I. Pulkkinen, V. Angelopoulos, W. Baumjohann, and R. L. McPherron (1996), Neutral line model of substorms: Past results and present view, *J. Geophys. Res.*, *101*(A6), 12,975–13,010, doi:10.1029/95JA03753.

Bruntz, R., R. E. Lopez, M. Wiltberger, and J. G. Lyon (2012), Investigation of the viscous potential using an MHD simulation, *J. Geophys. Res.*, *117*, A03214, doi:10.1029/2011JA017022.

Burke, W. J., and N. C. Maynard (1999), Geoeffective interplanetary scale sizes derived from regression analysis of polar cap potentials, *J. Geophys. Res.*, *104*(A5), 9989–9994, doi:10.1029/1999JA900031.

Burke, W. J., M. C. Kelley, R. C. Sagalyn, M. Smiddy, and S. T. Lai (1979), Polar cap electric field structures with a northward interplanetary magnetic field, *Geophys. Res. Lett.*, *6*, 21–24, doi:10.1029/GL006i001p00021.

Claudepierre, S. G., S. R. Elkington, and M. Wiltberger (2008), Solar wind driving of magnetospheric ULF waves: Pulsations driven by velocity shear at the magnetopause, *J. Geophys. Res.*, *113*, A05218, doi:10.1029/2007JA012890.

Crooker, N. U. (1992), Reverse convection, *J. Geophys. Res.*, *97*(A12), 19,363–19,372, doi:10.1029/92JA01532.

Cumnock, J. A., R. A. Heelis, M. R. Hairston, and P. T. Newell (1995), High-latitude ionospheric convection pattern during steady northward interplanetary magnetic field, *J. Geophys. Res.*, *100*(A8), 14,537–14,555, doi:10.1029/94JA03318.

DeJong, A. D., X. Cai, R. C. Clauer, and J. F. Spann (2007), Aurora and open magnetic flux during isolated substorms, sawteeth, and SMC events, *Ann. Geophys.*, *25*, 1865–1876, doi:10.5194/angeo-25-1865-2007.

Dungey, J. W. (1961), Interplanetary magnetic field and auroral zones, *Phys. Rev. Lett.*, *6*, 47–48, doi:10.1103/PhysRevLett.6.47.

Fedder, J. A., and J. G. Lyon (1995), The Earth's magnetosphere is 165 R_E long: Self-consistent currents, convection, magnetospheric structure, and processes for northward interplanetary magnetic field, *J. Geophys. Res.*, *100*(A3), 3623–3635, doi:10.1029/94JA02633.

Fedder, J., S. Slinker, J. Lyon, and R. Elphinstone (1995), Global numerical simulation of the growth phase and the expansion onset for a substorm observed by Viking, *J. Geophys. Res.*, *100*(A10), 19,083–19,093, doi:10.1029/95JA01524.

Gonzalez, W. D., J. A. Joselyn, Y. Kamide, H. W. Kroehl, G. Rostoker, B. T. Tsurutani, and V. M. Vasyliunas (1994), What is a geomagnetic storm?, *J. Geophys. Res.*, *99*(A4), 5771–5792, doi:10.1029/93JA02867.

Hairston, M. R., T. W. Hill, and R. A. Heelis (2003), Observed saturation of the ionosphere polar cap potential during the 31 March 2001 storm, *Geophys. Res. Lett.*, *30*(6), 1325, doi:10.1029/2002GL015894.

Hill, T. W. (1994), Theoretical models of polar-cap convection under the influence of a northward interplanetary magnetic field, *J. Atmos. Terr. Phys.*, *56*(2), 185–194, doi:10.1016/0021-9169(94)90029-9.

Hill, T. W., A. J. Dessler, and R. A. Wolf (1976), Mercury and Mars: The role of ionospheric conductivity in the acceleration of magnetospheric particles, *Geophys. Res. Lett.*, *3*, 429–432, doi:10.1029/GL003i008p00429.

Huang, C.-S., D. Andre, G. J. Sofko, and A. V. Koustov (2000), Super Dual Auroral Radar Network observations of ionospheric multicell convection during northward interplanetary magnetic field, *J. Geophys. Res.*, *105*(A4), 7419–7428, doi:10.1029/1999JA000364.

Iijima, T., and T. A. Potemra (1976), The amplitude distribution of field-aligned currents at northern high latitudes observed by TRIAD, *J. Geophys. Res.*, *81*(13), 2165–2174, doi:10.1029/JA081i013p02165.

Iijima, T., and T. Shibaji (1987), Global characteristics of northward IMF-associated (NBZ) field-aligned currents, *J. Geophys. Res.*, *92*(A3), 2408–2424, doi:10.1029/JA092iA03p02408.

Kivelson, M. G., and A. J. Ridley (2008), Saturation of the polar cap potential: Inference from Alfvén wing arguments, *J. Geophys. Res.*, *113*, A05214, doi:10.1029/2007JA012302.

Liemohn, M. W., J. U. Kozyra, M. R. Hairston, D. M. Weimer, G. Lu, A. J. Ridley, T. H. Zurbuchen, and R. M. Skoug (2002), Consequences of a saturated convection electric field on the ring current, *Geophys. Res. Lett.*, *29*(9), 1348, doi:10.1029/2001GL014270.

Lopez, R. E., C. C. Goodrich, G. D. Reeves, R. D. Belian, and A. Taktakishvili (1994), Midtail plasma flows and the relationship to near-Earth substorm activity: A case study, *J. Geophys. Res.*, *99*(A12), 23,561–23,569, doi:10.1029/94JA01771.

Lopez, R. E., M. Wiltberger, J. G. Lyon, C. C. Goodrich, and K. Papadopoulos (1999), MHD simulations of the response of high-latitude potential patterns and polar cap boundaries to sudden southward turnings of the interplanetary magnetic field, *Geophys. Res. Lett.*, *26*, 967–970, doi:10.1029/1999GL900113.

Lopez, R. E., M. Wiltberger, S. Hernandez, and J. G. Lyon (2004), Solar wind density control of energy transfer to the magnetosphere, *Geophys. Res. Lett.*, *31*, L08804, doi:10.1029/2003GL018780.

Lopez, R. E., S. Hernandez, M. Wiltberger, C.-L. Huang, E. L. Kepko, H. Spence, C. C. Goodrich, and J. G. Lyon (2007), Predicting magnetopause crossings at geosynchronous orbit during the Halloween storms, *Space Weather*, *5*, S01005, doi:10.1029/2006SW000222.

Lopez, R. E., J. G. Lyon, E. Mitchell, R. Bruntz, V. G. Merkin, S. Brogl, F. Toffoletto, and M. Wiltberger (2009), Why doesn't the ring current injection rate saturate?, *J. Geophys. Res.*, *114*, A02204, doi:10.1029/2008JA013141.

Lopez, R. E., R. J. Bruntz, E. J. Mitchell, M. Wiltberger, and J. G. Lyon (2010), The role of magnetosheath force balance in regulating the dayside reconnection potential, *J. Geophys. Res.*, *115*, A12216, doi:10.1029/2009JA014597.

Lopez, R. E., S. K. Bhattarai, R. Bruntz, K. Pham, M. Wiltberger, J. G. Lyon, Y. Deng, and Y. Huang (2012), The role of dayside merging in generating the ionospheric potential during the whole heliosphere interval, *J. Atmos. Sol. Terr. Phys.*, doi:10.1016/j.jastp.2012.03.001, in press.

Lui, A. T. Y. (2009), Comment on "Tail reconnection triggering substorm onset," *Science*, *324*, 1391, doi:10.1126/science.1167726.

Lyon, J., R. E. Lopez, C. C. Goodrich, M. Wiltberger, and K. Papadopoulos (1998), Simulation of the March 9, 1995, substorm: Auroral brightening and the onset of lobe reconnection, *Geophys. Res. Lett.*, *25*(15), 3039–3042, doi:10.1029/98GL00662.

Lyon, J. G., J. A. Feeder, and C. M. Mobarry (2004), The Lyon-Feeder-Mobarry (LFM) global MHD magnetospheric simulation code, *J. Atmos. Sol. Terr. Phys.*, *66*, 1333–1350, doi:10.1016/j.jastp.2004.03.020.

Merkin, V. G., J. G. Lyon, B. J. Anderson, H. Korth, C. C. Goodrich, and K. Papadopoulos (2007), A global MHD simulation of an event with a quasi-steady northward IMF component, *Ann. Geophys.*, *25*, 1345–1358, doi:10.5194/angeo-25-1345-2007.

Merkine, V. G., K. Papadopoulos, G. Milikh, A. S. Sharma, X. Shao, J. Lyon, and C. Goodrich (2003), Effects of the solar wind electric field and ionospheric conductance on the cross polar cap potential: Results of global MHD modeling, *Geophys. Res. Lett.*, *30*(23), 2180, doi:10.1029/2003GL017903.

Mitchell, E. J., R. E. Lopez, R. J. Bruntz, M. Wiltberger, J. G. Lyon, R. C. Allen, S. J. Cockrell, and P. L. Whittlesey (2010), Saturation of transpolar potential for large *Y* component interplanetary magnetic field, *J. Geophys. Res.*, *115*, A06201, doi:10.1029/2009JA015119.

Newell, P. T., T. Sotirelis, K. Liou, and F. J. Rich (2008), Pairs of solar wind-magnetosphere coupling functions: Combining a merging term with a viscous term works best, *J. Geophys. Res.*, *113*, A04218, doi:10.1029/2007JA012825.

Ober, D. M., N. C. Maynard, and W. J. Burke (2003), Testing the Hill model of transpolar potential saturation, *J. Geophys. Res.*, *108*(A12), 1467, doi:10.1029/2003JA010154.

Otto, A., and D. Fairfield (2000), Kelvin-Helmholtz instability at the magnetotail boundary: MHD simulation and comparison with Geotail observations, *J. Geophys. Res.*, *105*(A9), 21,175–21,190, doi:10.1029/1999JA000312.

Raeder, J., Y. L. Wang, T. J. Fuller-Rowell, and H. J. Singer (2001), Global simulation of space weather effects on the Bastille Day storm, *Sol. Phys.*, *204*, 323–337, doi:10.1023/A:1014228230714.

Ridley, A. J. (2007), Alfvén wings at Earth's magnetosphere under strong interplanetary magnetic field, *Ann. Geophys.*, *25*, 533–542, doi:10.5194/angeo-25-533-2007.

Ruohoniemi, J. M., and R. A. Greenwald (1996), Statistical patterns of high-latitude convection obtained from Goose Bay HF radar observations, *J. Geophys. Res.*, *101*(A10), 21,743–21,763, doi:10.1029/96JA01584.

Russell, C. T., J. G. Luhmann, and G. Lu (2001), Nonlinear response of the polar ionosphere to large values of the interplanetary electric field, *J. Geophys. Res.*, *106*(A9), 18,495–18,504, doi:10.1029/2001JA900053.

Shepherd, S. G., R. A. Greenwald, and J. M. Ruohoniemi (2002), Cross polar cap potentials measured with Super Auroral Radar Network during quasi-steady solar wind and interplanetary magnetic field conditions, *J. Geophys. Res.*, *107*(A7), 1094, doi:10.1029/2001JA000152.

Siscoe, G. L., G. M. Erickson, B. U. O. Sonnerup, N. C. Maynard, J. A. Schoendorf, K. D. Siebert, D. R. Weimer, W. W. White, and G. R. Wilson (2002a), Hill model of transpolar potential saturation: Comparisons with MHD simulations, *J. Geophys. Res.*, *107*(A6), 1075, doi:10.1029/2001JA000109.

Siscoe, G. L., N. U. Crooker, and K. D. Siebert (2002b), Transpolar potential saturation: Roles of Region 1 current system and solar wind ram pressure, *J. Geophys. Res.*, *107*(A10), 1321, doi:10.1029/2001JA009176.

Sundberg, K. Å. T., J. A. Cumnock, and L. G. Bloomberg (2009a), Reverse convection potential: A statistical study of the general properties of lobe reconnection and saturation effects during northward IMF, *J. Geophys. Res.*, *114*, A06205, doi:10.1029/2008JA013838.

Sundberg, K. Å. T., L. G. Blomberg, and J. A. Cumnock (2009b), Properties of the boundary layer potential for northward interplanetary magnetic field, *Geophys. Res. Lett.*, *36*, L11104, doi:10.1029/2009GL038625.

Vasyliūnas, V. M. (2001), Electric field and plasma flow: What drives what?, *Geophys. Res. Lett.*, *28*(11), 2177–2180, doi:10.1029/2001GL013014.

Watanabe, M., and G. J. Sofko (2009), The interchange cycle: A fundamental mode of magnetic flux circulation for northward interplanetary magnetic field, *Geophys. Res. Lett.*, *36*, L03107, doi:10.1029/2008GL036682.

Wilder, F. D., C. R. Clauer, and J. B. H. Baker (2008), Reverse convection potential saturation during northward IMF, *Geophys. Res. Lett.*, *35*, L12103, doi:10.1029/2008GL034040.

Wilder, F. D., C. R. Clauer, and J. B. H. Baker (2009), Reverse convection potential saturation during northward IMF under various driving conditions, *J. Geophys. Res.*, *114*, A08209, doi:10.1029/2009JA014266.

Wilder, F. D., C. R. Clauer, and J. B. H. Baker (2010), Polar cap electric field saturation during interplanetary magnetic field B_z north and south conditions, *J. Geophys. Res.*, *115*, A10230, doi:10.1029/2010JA015487.

Wiltberger, M., T. S. Weigel, M. Gehmeyr, and T. Guild (2005), Analysis and visualization of space science model output and data with CISM-DX, *J. Geophys. Res.*, *110*, A09224, doi:10.1029/2004JA010956.

Wolf, R. A. (1995), Magnetospheric configuration, in *Introduction to Space Physics*, edited by M. G. Kivelson and C. T. Russell, pp. 288–329, Cambridge Univ. Press, Cambridge, U. K.

S. K. Bhattarai, R. Bruntz, and R. E. Lopez, Department of Physics, University of Texas at Arlington, Arlington, TX 76019, USA. (shreekrishna.bhattarai@mavs.uta.edu)

J. G. Lyon, Department of Physics and Astronomy, Dartmouth College, Hanover, NH 03755, USA.

M. Wiltberger, High Altitude Observatory, National Center for Atmospheric Research, Boulder, CO 80301, USA.